

Reentrant quantum anomalous Hall effect in molecular beam epitaxy-grown MnBi_2Te_4 thin films

Yuanzhao Li^{1,2,†}, Yunhe Bai^{2,†}, Yang Feng^{1,†*}, Jianli Luan^{1,2,†}, Zongwei Gao¹, Yang Chen², Yitian Tong², Ruixuan Liu², Su Kong Chong^{1,3}, Kang L. Wang^{3,4}, Xiaodong Zhou^{5,6,7}, Jian Shen^{5,6,7,8,9}, Jinsong Zhang^{2,14,15}, Yayu Wang^{2,14,15}, Chui-Zhen Chen^{10,11}, XinCheng Xie^{6,12,15}, Xiao Feng^{1,2,14,15*}, Ke He^{1,2,14,15*}, and Qi-Kun Xue^{1,2,13,14,15}

¹Beijing Academy of Quantum Information Sciences, Beijing 100193, China.

²State Key Laboratory of Low Dimensional Quantum Physics and Department of Physics, Tsinghua University, Beijing 100084, China.

³Department of Electrical and Computer Engineering, University of California Los Angeles, Los Angeles, California 90095, USA.

⁴Department of Physics and Astronomy, University of California Los Angeles, Los Angeles, California 90095, USA.

⁵State Key Laboratory of Surface Physics and Department of Physics, Fudan University, Shanghai 200438, China.

⁶Institute for Nanoelectronic Devices and Quantum Computing, Fudan University, Shanghai 200438, China.

⁷Zhangjiang Fudan International Innovation Center, Fudan University, Shanghai 201210, China.

⁸Shanghai Research Center for Quantum Sciences, Shanghai 201315, China.

⁹Collaborative Innovation Center of Advanced Microstructures, Nanjing 210093, China.

¹⁰School of Physical Science and Technology, Soochow University, Suzhou 215006, China.

¹¹Institute for Advanced Study, Soochow University, Suzhou 215006, China.

¹²International Center for Quantum Materials, School of Physics, Peking University, Beijing 100871, China.

¹³Southern University of Science and Technology, Shenzhen 518055, China.

¹⁴Frontier Science Center for Quantum Information, Beijing 100084, China.

¹⁵Hefei National Laboratory, Hefei 230088, P. R. China.

*Corresponding author. Email : fengyang@baqis.ac.cn ; xiaofeng@mail.tsinghua.edu.cn ; kehe@tsinghua.edu.cn

†These authors contributed equally to this work.

Abstract

In the realm of topological quantum physics, it is widely accepted that a global bandgap is necessary to achieve quantized Hall conductance, irrespective of its origin—magnetic field, exchange coupling or other mechanisms. A material exhibiting the quantum anomalous Hall (QAH) effect had been considered equivalent to a Chern insulator, a band insulator with non-zero Chern number. However, a **Chern Anderson insulator** (CAI), which arises in a conducting state with exchange-induced Berry curvature splitting and disorder-induced Anderson localization, can in principle exhibit the QAH effect. In this study, we investigate intrinsic magnetic topological insulator MnBi_2Te_4 thin films grown by molecular beam epitaxy (MBE). We observe a reentrant QAH effect when the Fermi energy enters the valence band and magnetic field equals zero, indicating the emergence of the CAI state. The discovery opens a new avenue for realizing the QAH effect and underscores the fundamental role of both Berry curvature and Anderson localization.

Main text

The quantum anomalous Hall (QAH) effect displays quantized Hall conductance and vanishing longitudinal one in the absence of external magnetic field [1]. After its first realization in a magnetic topological insulator (MTI) Cr-doped $(\text{Bi,Sb})_2\text{Te}_3$ [2], intensive efforts have been made to improve the sample quality by reducing the inevitable randomness of magnetic dopants. The QAH effect has been reproduced in various systems, such as MTI with modulation magnetic doping [3], MTI with various magnetic dopants [4,5], intrinsic MTI [6], two-dimensional (2D) moiré superlattice without magnetic elements [7–10], and spin-orbit proximitized graphene [11,12]. More recently, the fractional counterpart of QAH effect has been observed in twisted transition metal dichalcogenide layers [13,14] and high-quality graphene-based moiré superlattices [15], which offers an unprecedented opportunity to investigate strongly correlated topological electronic states. The materials with topologically protected quantum state, combined with properties such as the inherent spin-momentum locking, may lead to new device concepts for electronic applications.

The MnBi_2Te_4 [16–20] is anticipated to significantly enhance the magnetism with its high concentration and ordered magnetic atoms. The material has an A-type antiferromagnetic (AFM) order, resulting from the coupling of intralayer ferromagnetic (FM) and interlayer AFM. Consequently, thin odd-layer MnBi_2Te_4 possesses an uncompensated magnetization, and is expected to exhibit QAH effect at high temperatures, owing to its topologically nontrivial band structure with a large exchange gap [17,18]. However, the zero-magnetic-field (ZMF) QAH effect is seldom observed in few-odd-layer MnBi_2Te_4 , and the predicted large gap for the QAH state (~ 50 meV) has not been identified in spectroscopy [21–25]. The reason has been attributed to complex magnetic phases [26], multidomain structure [23,27], anti-site defects [28–31], or nonuniform thickness [32], but no consensus is concluded. The situation has recently led to speculation that the ZMF-state of five-layer MnBi_2Te_4 in most samples, with large longitudinal resistance and small Hall signal, might be a topologically trivial insulator [33] due to magnetic disorder. The robustness of the QAH effect and its relation to the Berry curvature, magnetism, and electronic ground states in the ZMF-state of MnBi_2Te_4 remain largely mysterious.

In this work, we investigate molecular beam epitaxy (MBE)-grown MnBi_2Te_4 thin films which show the QAH state at high magnetic field and become topologically trivial at zero magnetic field. Surprisingly, the films reenter the QAH state when the Fermi level is tuned into the valence band. More importantly, in contrast to the conventional wisdom that a QAH system exhibiting nonzero integer Hall conductance must be a Chern insulator with global bandgap [1,32], the observed reentrant QAH effect occurs in a gapless system subject to Anderson localization [34,35] which can thus be called a Chern Anderson insulator (CAI).

As a matter of fact, the stability of topological states against local perturbations is protected by an energy gap, irrespective of whether the bandgap is induced by external magnetic field [36,37], exchange coupling with local magnetic moments [38,39], or complex interplay between correlation effect and hopping interactions [40–44]. Otherwise the system under adiabatic evolution [45] will

undergo a topological phase transition when the gap between different eigenstates closes. Specifically, in the thin films of a time-reversal symmetry (TRS) protected three-dimensional topological insulator [46], the gapless top and bottom surface states are weakly hybridized through tunneling effect and double-degenerated [38]. The formation of long-range magnetic order brings the exchange coupling between electron spins and local moments of magnetic ions, which leads to the exchange-induced band splitting between different components of spin texture and gap opening near the Dirac point (DP) [38]. If the initial hybridized surface bands are already inverted, a sufficiently large average exchange energy (E_{ex}) will release the inversion between the inner pair of bands, but enlarge the band inversion between the outer pair (Fig. 1A). In this situation, the Berry curvature carried by the inner pair of bands (Ω_{in}) almost vanishes completely, while the other (Ω_{out}) has nonzero values in its spectrum (Fig. 1B). Correspondingly, the inner-bands-carried Chern number (C_{in}) defined as integral of Ω_{in} [47] keeps zero, but the outer-bands-carried Chern number (C_{out}) has nontrivial value within the final outer gap (Fig. 1C). This suggests the formation of a Chern insulator state with the presence of the QAH effect [38] when the Fermi energy (E_F) lies inside the global bandgap (grey shaded area, V_0).

Such a Chern insulator state is observed under the high-magnetic-field (HMF) polarized FM order in our MnBi_2Te_4 thin films, which are grown on sapphire substrate with *in-situ* oxygen exposure and post-annealing process as described in our previous work [48]. Figure 1D displays gate voltage (V_g) dependence of Hall resistivity (ρ_{yx}) and longitudinal resistivity (ρ_{xx}) of the five-layer thin film #1 performed at -9 T and 20 mK. Within the V_g range from -6 V to -3.5 V as denoted by the grey shaded area, the wide ρ_{yx} plateau with a mean of $1.0002 h/e^2$ and the vanishing ρ_{xx} with a mean of $0.0018 h/e^2$ characterize an HMF-QAH effect, which is consistent with previous reports in thin flakes [6,49,50,33]. Hereinafter we assign -5 V as the charge neutral point (CNP) of HMF-QAH regime, which corresponds to V_0 inside the global bandgap in Fig. 1C. Notably, $\rho_{xx} = 0.0018 h/e^2$ (46.2Ω) at V_0 is dramatically reduced from 5.16 k Ω previously reported in MnBi_2Te_4 thin films [48], indicating a significant improvement of the sample quality. In the range from -10.5 V to -8.5 V denoted by the gold shaded area away from V_0 , the simultaneously increasing ρ_{xx} and reducing ρ_{yx} indicate breakdown of HMF-QAH effect when E_F leaves the global bandgap.

However, the sufficiently large E_{ex} is not naturally fulfilled under the A-type AFM order of MnBi_2Te_4 [47] due to spatial nonuniformity of magnetization and reduction of E_{ex} by anti-site defects [28–31]. As suggested by a practical model for MTI [35], a nuanced yet significant scenario emerges when the average E_{ex} is weak relative to magnetic disorder. Figure 1E illustrates the band structure, where both inner and outer pairs of hybridized bands remain inverted due to weak exchange-induced splitting and the final gaps are topologically nontrivial. The contribution to both Ω_{in} and Ω_{out} primarily originates from the states near Γ point with small momentum in k -space, and are likely to be confined within a narrow energy range [47]. This results in a peak in the Berry curvature spectrum near the band edge (Fig. 1F). Given the electron-hole asymmetry that the energy dispersion of surface states in the $(\text{Bi, Sb})_2\text{Te}_3$ materials below the DP is smaller than that above the DP, the separation of Ω_{in} and Ω_{out} peaks due to band splitting below the DP in valence band is more pronounced. Simultaneously, the total Chern number $C = C_{in} + C_{out}$ no longer equals nontrivial integer at V_0 (Fig.

1G). Instead, $C = 1$ when E_F enters the valence band, as indicated by the gold shaded area (V_Ω). Ultimately, the exchange-induced Berry curvature splitting and disorder-induced Anderson localization can, in principle, give rise to a Chern Anderson insulator (CAI) state without a global bandgap. This state is marked by r-QAH effect, which refers to a QAH effect at 0 T and V_Ω [35] that is experimentally observed in this work.

To understand the observed ZMF-QAH effect, we investigate its V_g -dependent ρ_{yx} and ρ_{xx} at 20 mK in Fig. 1H. A maximum of $\rho_{xx} \approx 4.4 h/e^2$ appears at -4.7 V, indicating that the range marked by the gray shaded area around -5 V indeed corresponds to the global bandgap where conduction is mostly prohibited. The suppression of conduction is also reflected in the noisy ρ_{yx} in the same gate range. Intriguingly, the overall profile of ZMF ρ_{yx} with respect to V_g is very similar to the energy spectrum of C in Fig. 1G. Within the range from -10.5 V to -8.5 V denoted by the gold shaded area, ρ_{yx} arises and ultimately exhibits a nearly quantized plateau, indicating a ZMF-QAH effect when E_F enters the valence band. In other words, the r-QAH effect is obtained in the MnBi_2Te_4 thin film. We assign -9.5 V to the center of the r-QAH regime, corresponding to V_Ω in Fig. 1G. This r-QAH effect is further confirmed by the simultaneous decrease of ρ_{xx} from the maximum near V_0 to a dip ($\rho_{xx} \approx 0.85 h/e^2$) near V_Ω . Furthermore, the occurrence of r-QAH effect at 0 T and V_Ω is also consistent with the electron-hole asymmetry in $(\text{Bi, Sb})_2\text{Te}_3$ materials as emphasized in Fig. 1E. An immediate interpretation of these results is that the QAH effect can emerge from conducting states, signifying the transition from an ZMF-insulating state at V_0 to a CAI state at V_Ω .

Shown in Figure 2 is the magnetic field ($\mu_0 H$) dependence of ρ_{yx} and ρ_{xx} at V_0 and V_Ω . For the V_0 case, the HMF-QAH effect is further confirmed in range $6 \text{ T} < |\mu_0 H| < 9 \text{ T}$, seen by fully quantized ρ_{yx} with a mean of $1.0004 h/e^2$ in Fig. 2A and a vanishing ρ_{xx} with a mean of 41.0Ω ($\approx 0.0016 h/e^2$) in Fig. 2B. As $\mu_0 H$ decreases, ρ_{yx} deviates from the quantized plateau, whereas ρ_{xx} increases monotonously, illustrating a transition from HMF-FM-QAH state to a ZMF-AFM-insulating one. The latter has two typical features: one is the hysteretic ρ_{yx} and ρ_{xx} with coercivity $\mu_0 H_c = 0.90 \text{ T}$ due to the finite net magnetization corresponding to the odd-layer number; the other is a ZMF $|\rho_{yx}| \approx 0.6 h/e^2$ and a large $\rho_{xx} \approx 7.6 h/e^2$, indicating the breakdown of QAH effect.

For the V_Ω case, the $\mu_0 H$ -dependent ρ_{yx} and ρ_{xx} in Fig. 2C and Fig. 2D undoubtedly confirms the reentrance picture. The entire demagnetization process can be divided into several stages. The first stage is the reinforcing process from $\pm 9 \text{ T}$ to $\pm 7.2 \text{ T}$ (orange ticks), in which $|\rho_{yx}|$ persists full quantization while ρ_{xx} drops from $\rho_{xx} \approx 0.07 h/e^2$ to $\rho_{xx} \approx 0.04 h/e^2$. The second stage is the rapid-weakening process from $\pm 7.2 \text{ T}$ (orange ticks) to $\pm 3.8 \text{ T}$ (red ticks), in which the perfect quantization drops off to $|\rho_{yx}| \approx 0.9 h/e^2$ and ρ_{xx} rapidly increases up to $\rho_{xx} \approx 1.0 h/e^2$. The third stage is the gradual-weakening process from $\pm 3.8 \text{ T}$ (red ticks) to $\pm 2.1 \text{ T}$ (green ticks), in which $|\rho_{yx}|$ is further reduced to $|\rho_{yx}| \approx 0.8 h/e^2$ and ρ_{xx} keeps increasing to $\rho_{xx} \approx 1.3 h/e^2$. The last stage is the reentering process from $\pm 2.1 \text{ T}$ (green ticks) to 0 T, at the end of which $|\rho_{yx}|$ regains a nearly quantized value $0.9736 h/e^2$, which represents the most important finding of this work. Note that, the ZMF $\rho_{xx} = 1.0756 h/e^2$ in Fig. 2D is larger than $\rho_{xx} \approx 0.85 h/e^2$ at V_Ω in Fig. 1H, which is likely caused by the heating effect during the $\mu_0 H$ sweep process. For comparison, ZMF ρ_{yx} and ρ_{xx} of the QAH effect in the exfoliated MnBi_2Te_4 thin

flake is $0.97 h/e^2$ and $0.061 h/e^2$, respectively [6].

To further explore the r-QAH effect, we systematically compare the transport behavior of the ZMF-insulating state (0 T and V_0) and the CAI state (0 T and V_Ω). Fig 3A (3B) show the temperature (T) dependence of ZMF ρ_{yx} and ρ_{xx} at V_0 (V_Ω). In both cases, ρ_{yx} exhibits larger value at lower T , but the trend of ρ_{xx} is different. The ZMF-insulating state displays a diverging ρ_{xx} as T approaches zero. In contrast, the CAI state shows a metallic behavior below 0.5 K, as characterized by the reducing ρ_{xx} as T decreases. This provides additional evidence for the breakdown (reentrance) of QAH effect at V_0 (V_Ω).

Figure 3C and 3D present an instructive analysis by plotting the μ_0H -dependent tangent of the Hall angle θ_H , defined as $\tan\theta_H = \sigma_{xy}/\sigma_{xx} = \rho_{yx}/\rho_{xx}$ [51], where σ_{xy} (σ_{xx}) denotes Hall (longitudinal) conductivity. For V_0 case (Fig. 3C), $\tan\theta_H$ decays monotonously from a large value exceeding 400 (indicative of HMF-QAH effect) to a small value below 0.1, suggesting a ZMF-insulating state. This decayed Hall response with reducing μ_0H is consistent with the μ_0H -dependent ρ_{yx} at V_0 in Fig. 2A. In contrast, $\tan\theta_H$ at V_Ω (Fig. 3D) exhibits a non-monotonic behavior, in which four stages (reinforcing, rapid-weakening, gradual-weakening, and reentering) are clearly resolved. This multistage Hall response at V_Ω confirms the evolution from the HMF-QAH effect to the r-QAH effect, providing valuable insights into the formation of the CAI state.

To elucidate the energetics of the transport behavior, we employ line fits to the Arrhenius plots of $1/T$ -dependent σ_{xx} [47]. This yields the energy scale ΔE at V_0 (Fig. 3E) and V_Ω (Fig. 3F). It characterizes the minimum energy required to trigger the thermal excitation of electrons participating in global transport. When E_F lies inside the global bandgap, ΔE equals the spacing of nearest band edges. However, when E_F enters the valence band with the presence of disorder, ΔE describes the mobility gap. It is important to note that in the QAH regime, $\sigma_{xx} = \rho_{xx}/(\rho_{xx}^2 + \rho_{yx}^2)$ no longer equals $1/\rho_{xx}$, hence ΔE cannot reflect the metallic behavior (ρ_{xx} vs T) in Fig. 3B directly. The common feature in Fig. 3E and Fig. 3F is the minimum ΔE occurring near $|\mu_0H| = 3.8$ T (red tick), corresponding to the transition from HMF-FM order to ZMF-AFM order. On both sides of the red tick, ΔE shows monotonic changes at V_0 , but displays non-monotonic μ_0H evolution at V_Ω . Two important differences are particularly noted. First, an inflection point or maximum of ΔE , which is absent in V_0 case, appears at $|\mu_0H| = 7.2$ T (orange tick) in V_Ω case, closely resembling $|\mu_0H| \approx 7.6$ T in the exfoliated flake with ZMF-QAH effect [6]. Second, within the reentrant regime $|\mu_0H| < 2.1$ T, instead of increasing at V_0 , ΔE decreases as μ_0H approaches zero at V_Ω . Overall, the μ_0H evolution with four stages (marked by ticks) are consistent with μ_0H -dependent ρ_{yx} , ρ_{xx} , $\tan\theta_H$, and ΔE (Fig. 2 and Fig. 3), which shows contrasting behavior between V_0 and V_Ω case.

In Fig. 3G, we give a phase diagram in the intensity plot of ρ_{yx} as a function of μ_0H and V_g , offering a comprehensive view into the evolution of the QAH state in our system. The direction of μ_0H sweep is from -9 T to +9 T, as indicated by the black arrow. The HMF-QAH regimes primarily exist at $|\mu_0H| > 4$ T and $V_g < -2$ V. In contrast, the r-QAH regime, characterized by a strong rebuilding of $\rho_{yx} \approx 0.97 h/e^2$ only exists in a narrow range around 0 T and V_Ω (gold tick), consistent with the electron-hole

asymmetry (Fig. 1E and 1F). The presence of the r-QAH effect, as well as the ZFM-insulating state, is further revealed by the intensity plot of ρ_{xx} [47].

A more intuitive understanding of the r-QAH effect at 0 T and V_Ω can be gleaned by comparing film #1 with other ZMF results. In particular, we include three additional MBE-grown thin films #2, #3, #4 [47], a seven-layer exfoliated MnBi_2Te_4 thin flake #5 with pressure-enhanced ZMF-QAH effect [52], and a five-layer thin flake #6 exhibiting ZMF-QAH effect [6]. Fig. 4A displays the T -dependent $\tan\theta_H$ for all samples. Note that, except for #1, all the data in this plot is at each CNP (V_0). A contrasting behavior is observed between films (#2, #3, #4) and flakes (#5, #6). Specifically, as T approaches zero, the $\tan\theta_H$ curve of #2, #3, #4 decreases whereas those of #5, #6 diverge. Interestingly, the behavior of film #1 at V_0 aligns more closely with sample #2, #3, #4, whereas at V_Ω it shares similar upward trend with #5, #6. It strongly suggests that, the MnBi_2Te_4 thin film #1 undergoes a topological transition from a ZMF-insulating state to a CAI state exhibiting r-QAH effect with the aid of V_g .

We further undertake a scaling analysis of ZMF $\tan\theta_H$ with respect to T and ΔE . As depicted in Fig. 4B, all $\tan\theta_H$ versus $T/\Delta E^\alpha$ curves, both within the ZMF-insulating regime (#1@ V_0 , #2, #3, #4) and the QAH regime (#5, #6), coalesce into single curves with $\alpha \approx 0.6 \pm 0.05$. This excludes the extremely low T regime where lattice temperature and electron temperature typically decouple. The transition point can be obtained at $\tan\theta_H \approx 0.5$ where a T -independence is observed [53]. However, the $\tan\theta_H$ curves in the QAH regime (#5, #6) and the r-QAH regime (#1@ V_Ω) are not directly overlapped, leaving an open question of whether the r-QAH effect in the CAI state and the QAH effect in Chern insulator state [6,52] are entirely equivalent. One possible difference might be concealed in the fact that a bandgap and a mobility gap are not directly comparable. Nevertheless, future theoretical and experimental endeavors are needed to scrutinize such a CAI state and develop a proper theory describing its scaling behavior.

Figure. 4C provides another perspective to understand the CAI state by viewing the evolution in the parameter plot of conductivities ($\sigma_{xy}(\beta)$, $\sigma_{xx}(\beta)$), where β involves two parameters, T and V_g . We first analyze the ZMF behavior of samples prior to this work (#2 to #6) by examining the T -dependent conductivity (σ) tensor (dashed lines). Under the perspective of renormalization group (RG) flow, the σ tensor under broken TRS is suggested to flow towards critical points in the condition of diverging system size (L). Such condition is experimentally equivalent to cooling the system ($T \rightarrow 0$) where the inelastic scattering length or phase coherence length diverges. As T approaches zero, thin films #2, #3, #4 flow to $(0, 0)$ consistent with a ZMF-insulating state. Conversely, exfoliated thin flakes #5, #6 flow towards $(e^2/h, 0)$ as anticipated for a QAH state. These two resolved stable phases are consistent with previous work [54–56].

We further analyze the evolution of film #1 from V_0 to V_Ω denoted by solid line in Fig. 4C, which is adapted from Fig. 1H. It collapses onto a semicircle of radius $e^2/2h$ centered at $(e^2/2h, 0)$, consistent with the open circles extracted from $\mu_0 H$ sweeps in Fig. 3G. This recalls the semicircular law, which is expected as long as ρ_{yx} is quantized irrespective of ρ_{xx} [57,58], and has been utilized to describe the transition from the insulating state to a QAH state [56]. Clearly, in such a V_g -driven transition, σ tensor

flows from a ZMF-insulating state towards a QAH state and ends on the right side of $(e^2/2h, e^2/2h)$. Notably, the transition point (indicated by blue arrow) with T -independent $\tan\theta_H \approx 0.5$ obtained from Fig. 4B is not in the vicinity of $(e^2/2h, e^2/2h)$, as predicted by a modular symmetry group theory [59]. Similar asymmetric RG flow has been reported in MTI system [60] and even in an ideal quantum well sample with perfect semicircle relation [58]. The two distinct ground states of film #1 on both sides of transition point are also confirmed by their T -dependent σ flows at V_0 and V_Ω denoted by green and blue dashed lines in Fig. 4C.

In summary, we have observed the r-QAH effect in MBE-grown MnBi_2Te_4 thin films, which signifies the formation of the CAI state. Different from previously reported QAH states that relies on a global bandgap, the newly found QAH state exists in a conducting state with a moderate exchange level and weak disorder. The exchange-induced Berry curvature splitting and Anderson localization both contribute to this significant phenomenon. Our work not only paves a new path for realizing QAH effect, but also stimulates research to explore Berry curvature-related physical phenomena in multiband systems without a global bandgap. This includes chiral optical responses, topological plasmonic and excitonic polaritons in metals, semiconductors, and superconductors with unconventional pairing.

Acknowledgement

We thank Junjie Qi, Peng Deng, and Chang Liu for helpful discussions.

References

- [1] F. D. M. Haldane, *Model for a Quantum Hall Effect without Landau Levels: Condensed-Matter Realization of the "Parity Anomaly,"* Phys. Rev. Lett. **61**, 2015 (1988).
- [2] C.-Z. Chang et al., *Experimental Observation of the Quantum Anomalous Hall Effect in a Magnetic Topological Insulator,* Science **340**, 167 (2013).
- [3] M. Mogi, R. Yoshimi, A. Tsukazaki, K. Yasuda, Y. Kozuka, K. S. Takahashi, M. Kawasaki, and Y. Tokura, *Magnetic Modulation Doping in Topological Insulators toward Higher-Temperature Quantum Anomalous Hall Effect,* Applied Physics Letters **107**, 182401 (2015).
- [4] C.-Z. Chang, W. Zhao, D. Y. Kim, H. Zhang, B. A. Assaf, D. Heiman, S.-C. Zhang, C. Liu, M. H. W. Chan, and J. S. Moodera, *High-Precision Realization of Robust Quantum Anomalous Hall State in a Hard Ferromagnetic Topological Insulator,* Nat Mater **14**, 473 (2015).
- [5] Y. Ou et al., *Enhancing the Quantum Anomalous Hall Effect by Magnetic Codoping in a Topological Insulator,* Adv. Mater. **30**, 1703062 (2017).
- [6] Y. Deng, Y. Yu, M. Z. Shi, Z. Guo, Z. Xu, J. Wang, X. H. Chen, and Y. Zhang, *Quantum Anomalous Hall Effect in Intrinsic Magnetic Topological Insulator MnBi_2Te_4 ,* Science **367**, 895 (2020).

- [7] A. L. Sharpe, E. J. Fox, A. W. Barnard, J. Finney, K. Watanabe, T. Taniguchi, M. A. Kastner, and D. Goldhaber-Gordon, *Emergent Ferromagnetism near Three-Quarters Filling in Twisted Bilayer Graphene*, *Science* **365**, 605 (2019).
- [8] M. Serlin, C. L. Tschirhart, H. Polshyn, Y. Zhang, J. Zhu, K. Watanabe, T. Taniguchi, L. Balents, and Andrea. F. Young, *Intrinsic Quantized Anomalous Hall Effect in a Moiré Heterostructure*, *Science* **367**, 900 (2020).
- [9] G. Chen et al., *Tunable Correlated Chern Insulator and Ferromagnetism in a Moiré Superlattice*, *Nature* **579**, 56 (2020).
- [10] T. Li et al., *Quantum Anomalous Hall Effect from Intertwined Moiré Bands*, *Nature* **600**, 7890 (2021).
- [11] T. Han et al., *Large Quantum Anomalous Hall Effect in Spin-Orbit Proximitized Rhombohedral Graphene*, arXiv:2310.17483.
- [12] Y. Sha, J. Zheng, K. Liu, H. Du, K. Watanabe, T. Taniguchi, J. Jia, Z. Shi, R. Zhong, and G. Chen, *Observation of Chern Insulator in Crystalline ABCA-Tetralayer Graphene with Spin-Orbit Coupling*, arXiv:2310.17971.
- [13] H. Park et al., *Observation of Fractionally Quantized Anomalous Hall Effect*, *Nature* **1** (2023).
- [14] F. Xu et al., *Observation of Integer and Fractional Quantum Anomalous Hall Effects in Twisted Bilayer $MoTe_2$* , *Phys. Rev. X* **13**, 031037 (2023).
- [15] Z. Lu, T. Han, Y. Yao, A. P. Reddy, J. Yang, J. Seo, K. Watanabe, T. Taniguchi, L. Fu, and L. Ju, *Fractional Quantum Anomalous Hall Effect in a Graphene Moire Superlattice*, arXiv:2309.17436.
- [16] M. M. Otrokov, I. P. Rusinov, M. Blanco-Rey, M. Hoffmann, A. Yu. Vyazovskaya, S. V. Eremeev, A. Ernst, P. M. Echenique, A. Arnau, and E. V. Chulkov, *Unique Thickness-Dependent Properties of the van Der Waals Interlayer Antiferromagnet $MnBi_2Te_4$ Films*, *Phys. Rev. Lett.* **122**, 107202 (2019).
- [17] D. Zhang, M. Shi, T. Zhu, D. Xing, H. Zhang, and J. Wang, *Topological Axion States in the Magnetic Insulator $MnBi_2Te_4$ with the Quantized Magnetoelectric Effect*, *Phys. Rev. Lett.* **122**, 206401 (2019).
- [18] J. Li, Y. Li, S. Du, Z. Wang, B.-L. Gu, S.-C. Zhang, K. He, W. Duan, and Y. Xu, *Intrinsic Magnetic Topological Insulators in van Der Waals Layered $MnBi_2Te_4$ -Family Materials*, *Science Advances* **5**, eaaw5685 (2019).
- [19] Y. Gong et al., *Experimental Realization of an Intrinsic Magnetic Topological Insulator**, *Chinese Physics Letters* **36**, 076801 (2019).
- [20] M. M. Otrokov et al., *Prediction and Observation of an Antiferromagnetic Topological Insulator*, *Nature* **576**, 416 (2019).

- [21] Y.-J. Hao et al., *Gapless Surface Dirac Cone in Antiferromagnetic Topological Insulator $MnBi_2Te_4$* , Phys. Rev. X **9**, 041038 (2019).
- [22] H. Li et al., *Dirac Surface States in Intrinsic Magnetic Topological Insulators $EuSn_2As_2$ and $MnBi_{2n}Te_{3n+1}$* , Phys. Rev. X **9**, 041039 (2019).
- [23] Y. J. Chen et al., *Topological Electronic Structure and Its Temperature Evolution in Antiferromagnetic Topological Insulator $MnBi_2Te_4$* , Phys. Rev. X **9**, 041040 (2019).
- [24] P. Swatek, Y. Wu, L.-L. Wang, K. Lee, B. Schruck, J. Yan, and A. Kaminski, *Gapless Dirac Surface States in the Antiferromagnetic Topological Insulator $MnBi_2Te_4$* , Phys. Rev. B **101**, 161109 (2020).
- [25] D. Nevola, H. X. Li, J.-Q. Yan, R. G. Moore, H.-N. Lee, H. Miao, and P. D. Johnson, *Coexistence of Surface Ferromagnetism and a Gapless Topological State in $MnBi_2Te_4$* , Phys. Rev. Lett. **125**, 117205 (2020).
- [26] B. Li, J.-Q. Yan, D. M. Pajerowski, E. Gordon, A.-M. Nedić, Y. Sizyuk, L. Ke, P. P. Orth, D. Vaknin, and R. J. McQueeney, *Competing Magnetic Interactions in the Antiferromagnetic Topological Insulator $MnBi_2Te_4$* , Phys. Rev. Lett. **124**, 167204 (2020).
- [27] I. P. Rusinov, V. N. Men'shov, and E. V. Chulkov, *Spectral Features of Magnetic Domain Walls on the Surface of Three-Dimensional Topological Insulators*, Phys. Rev. B **104**, 035411 (2021).
- [28] Y. Lai, L. Ke, J. Yan, R. D. McDonald, and R. J. McQueeney, *Defect-Driven Ferrimagnetism and Hidden Magnetization in $MnBi_2Te_4$* , Phys. Rev. B **103**, 184429 (2021).
- [29] M. Garnica et al., *Native Point Defects and Their Implications for the Dirac Point Gap at $MnBi_2Te_4(0001)$* , Npj Quantum Mater. **7**, 1 (2022).
- [30] M. Liu, C. Lei, H. Kim, Y. Li, L. Frammolino, J. Yan, A. H. MacDonald, and C.-K. Shih, *Visualizing the Interplay of Dirac Mass Gap and Magnetism at Nanoscale in Intrinsic Magnetic Topological Insulators*, Proceedings of the National Academy of Sciences **119**, e2207681119 (2022).
- [31] H. Tan and B. Yan, *Distinct Magnetic Gaps between Antiferromagnetic and Ferromagnetic Orders Driven by Surface Defects in the Topological Magnet $MnBi_2Te_4$* , Phys. Rev. Lett. **130**, 126702 (2023).
- [32] C.-Z. Chang, C.-X. Liu, and A. H. MacDonald, *Colloquium: Quantum Anomalous Hall Effect*, Rev. Mod. Phys. **95**, 011002 (2023).
- [33] D. Ovchinnikov et al., *Intertwined Topological and Magnetic Orders in Atomically Thin Chern Insulator $MnBi_2Te_4$* , Nano Lett. **21**, 2544 (2021).
- [34] M. Onoda and N. Nagaosa, *Quantized Anomalous Hall Effect in Two-Dimensional Ferromagnets: Quantum Hall Effect in Metals*, Phys. Rev. Lett. **90**, 206601 (2003).
- [35] C.-Z. Chen, J. Qi, D.-H. Xu, and X. Xie, *Evolution of Berry Curvature and Reentrant Quantum*

Anomalous Hall Effect in an Intrinsic Magnetic Topological Insulator, Sci. China Phys. Mech. Astron. **64**, 127211 (2021).

- [36] K. v. Klitzing, G. Dorda, and M. Pepper, *New Method for High-Accuracy Determination of the Fine-Structure Constant Based on Quantized Hall Resistance*, Phys. Rev. Lett. **45**, 494 (1980).
- [37] D. J. Thouless, M. Kohmoto, M. P. Nightingale, and M. den Nijs, *Quantized Hall Conductance in a Two-Dimensional Periodic Potential*, Phys. Rev. Lett. **49**, 405 (1982).
- [38] R. Yu, W. Zhang, H.-J. Zhang, S.-C. Zhang, X. Dai, and Z. Fang, *Quantized Anomalous Hall Effect in Magnetic Topological Insulators*, Science **329**, 61 (2010).
- [39] C.-Z. Chang et al., *Thin Films of Magnetically Doped Topological Insulator with Carrier-Independent Long-Range Ferromagnetic Order*, Adv. Mater. **25**, 1065 (2013).
- [40] M. Xie and A. H. MacDonald, *Nature of the Correlated Insulator States in Twisted Bilayer Graphene*, Phys. Rev. Lett. **124**, 097601 (2020).
- [41] Y.-H. Zhang, D. Mao, and T. Senthil, *Twisted Bilayer Graphene Aligned with Hexagonal Boron Nitride: Anomalous Hall Effect and a Lattice Model*, Phys. Rev. Res. **1**, 033126 (2019).
- [42] Z. Tao et al., *Valley-Coherent Quantum Anomalous Hall State in AB-Stacked MoTe₂/WSe₂ Bilayers*, arXiv:2208.07452.
- [43] T. Devakul and L. Fu, *Quantum Anomalous Hall Effect from Inverted Charge Transfer Gap*, Phys. Rev. X **12**, 021031 (2022).
- [44] Y.-M. Xie, C.-P. Zhang, and K. T. Law, *Topological $P_x + iP_y$ Inter-Valley Coherent State in Moiré MoTe₂/WSe₂ Heterobilayers*, arXiv:2206.11666.
- [45] R. E. Prange and S. M. Girvin, editors, *The Quantum Hall Effect* (Springer New York, New York, NY, 1990).
- [46] H. Zhang, C.-X. Liu, X.-L. Qi, X. Dai, Z. Fang, and S.-C. Zhang, *Topological Insulators in Bi₂Se₃, Bi₂Te₃ and Sb₂Te₃ with a Single Dirac Cone on the Surface*, Nat Phys **5**, 438 (2009).
- [47] *See Supplementary Materials.*, (n.d.).
- [48] Y. Bai et al., *Quantized Anomalous Hall Resistivity Achieved in Molecular Beam Epitaxy-Grown MnBi₂Te₄ Thin Films*, National Science Review nwad189 (2023).
- [49] C. Liu, Y. Wang, H. Li, Y. Wu, Y. Li, J. Li, K. He, Y. Xu, J. Zhang, and Y. Wang, *Robust Axion Insulator and Chern Insulator Phases in a Two-Dimensional Antiferromagnetic Topological Insulator*, Nature Materials **19**, 5 (2020).
- [50] J. Ge, Y. Liu, J. Li, H. Li, T. Luo, Y. Wu, Y. Xu, and J. Wang, *High-Chern-Number and High-Temperature Quantum Hall Effect without Landau Levels*, National Science Review **7**, 1280 (2020).
- [51] R. Watanabe, R. Yoshimi, M. Kawamura, M. Mogi, A. Tsukazaki, X. Z. Yu, K. Nakajima, K. S.

- Takahashi, M. Kawasaki, and Y. Tokura, *Quantum Anomalous Hall Effect Driven by Magnetic Proximity Coupling in All-Telluride Based Heterostructure*, Appl. Phys. Lett. **115**, 102403 (2019).
- [52] S. K. Chong et al., *Pressure Tunable Quantum Anomalous Hall States in a Topological Antiferromagnet*, arXiv:2306.10325.
- [53] D. Shahar, D. C. Tsui, M. Shayegan, R. N. Bhatt, and J. E. Cunningham, *Universal Conductivity at the Quantum Hall Liquid to Insulator Transition*, Phys. Rev. Lett. **74**, 4511 (1995).
- [54] A. M. M. Pruisken, *Dilute Instanton Gas as the Precursor to the Integral Quantum Hall Effect*, Phys. Rev. B **32**, 2636 (1985).
- [55] N. Nagaosa, J. Sinova, S. Onoda, A. H. MacDonald, and N. P. Ong, *Anomalous Hall Effect*, Rev. Mod. Phys. **82**, 1539 (2010).
- [56] J. G. Checkelsky, R. Yoshimi, A. Tsukazaki, K. S. Takahashi, Y. Kozuka, J. Falson, M. Kawasaki, and Y. Tokura, *Trajectory of the Anomalous Hall Effect towards the Quantized State in a Ferromagnetic Topological Insulator*, Nat Phys **10**, 731 (2014).
- [57] A. M. Dykhne and I. M. Ruzin, *Theory of the Fractional Quantum Hall Effect: The Two-Phase Model*, Phys. Rev. B **50**, 2369 (1994).
- [58] M. Hilke, D. Shahar, S. H. Song, D. C. Tsui, Y. H. Xie, and M. Shayegan, *Semicircle: An Exact Relation in the Integer and Fractional Quantum Hall Effect*, EPL **46**, 775 (1999).
- [59] B. P. Dolan, *Modular Symmetry and Temperature Flow of Conductivities in Quantum Hall Systems with Varying Zeeman Energy*, Phys. Rev. B **82**, 195319 (2010).
- [60] Y. Ji et al., *Thickness-Driven Quantum Anomalous Hall Phase Transition in Magnetic Topological Insulator Thin Films*, ACS Nano **16**, 1134 (2022).

Figures

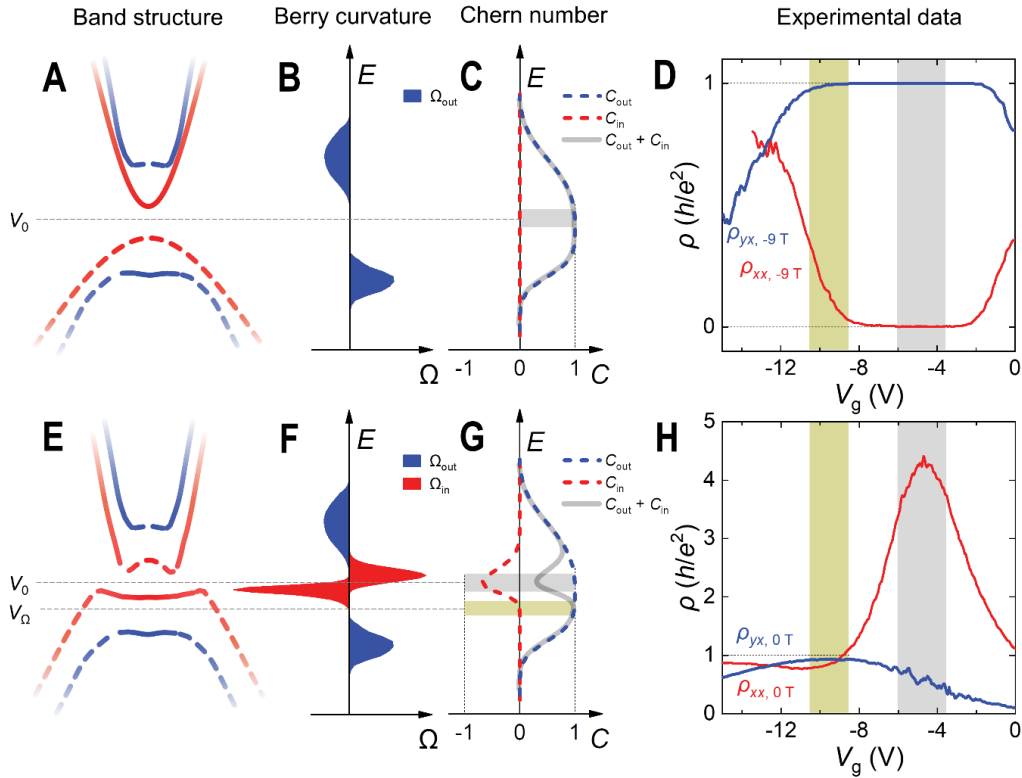


Fig. 1. Scheme of band structure, Berry curvature, Chern number and experimental performance of an MTI upon reducing the E_{ex} . The initial bands without E_{ex} are topologically nontrivial and double degenerated. Red or blue color denotes different component of spin texture. The solid or dashed line denotes the opposite parity at Γ point. E_{ex} draws the inner pair of bands (red) closer and pushes the outer pair (blue) farther away. The different energy dispersions of conduction and valence bands are due to the electron-hole asymmetry in MTI. **(A)** Band structure with strong E_{ex} . A large enough E_{ex} releases the nontrivial gap between the inner pair of bands. **(B)** The spin-resolved Berry curvature carried by inner and outer bands (Ω_{in} and Ω_{out}) with strong E_{ex} . Ω_{in} vanishes, but Ω_{out} is nonzero with two opposite peaks. **(C)** The spin-resolved Chern number (C_{in} and C_{out}) with strong E_{ex} . C_{in} vanishes but C_{out} is nonzero. The grey shaded area (V_0) denotes the CNP inside the global bandgap, which exhibits a Chern insulator state marked by a QAH effect $\sigma_{xy} = (C_{\text{in}} + C_{\text{out}}) e^2/h = e^2/h$. **(D)** V_g -dependent ρ_{yx} and ρ_{xx} of film #1 acquired at $\mu_0 H = -9$ T. The grey shaded area denotes HMF-QAH regime (-6 V, -3.5 V). $V_0 = -5$ V is assigned to the CNP of HMF-QAH regime. **(E)** Band structure with weak E_{ex} . Both pairs of bands remain topologically nontrivial, with the presence of magnetic disorder and insufficient E_{ex} . **(F)** Spin-resolved Berry curvature with weak E_{ex} . Both Ω_{in} and Ω_{out} have two opposite peaks. **(G)** Spin-resolved Chern number with weak E_{ex} . Both C_{in} and C_{out} are nonzero. At V_0 inside the gap, $C_{\text{in}} + C_{\text{out}} \neq 1$. The gold shaded area denotes the CAI regime (V_Ω), which refers to a conducting state with exchange-induced Berry curvature splitting and disorder-induced localization, marked by a r-QAH effect $C_{\text{in}} + C_{\text{out}} = 1$. **(H)** V_g -dependent ρ_{yx} and ρ_{xx} of film #1 acquired at $\mu_0 H = 0$ T. Within (-6 V, -3.5 V), the ZMF ρ_{yx} is noisy, and the maximum $\rho_{xx} \approx 4.4 h/e^2$ appears at -4.7 V, suggesting a ZMF-insulating state. The gold shaded area denotes the r-QAH regime (-10.5 V, -8.5 V). $V_\Omega = -9.5$ V is assigned to the center of the r-QAH regime.

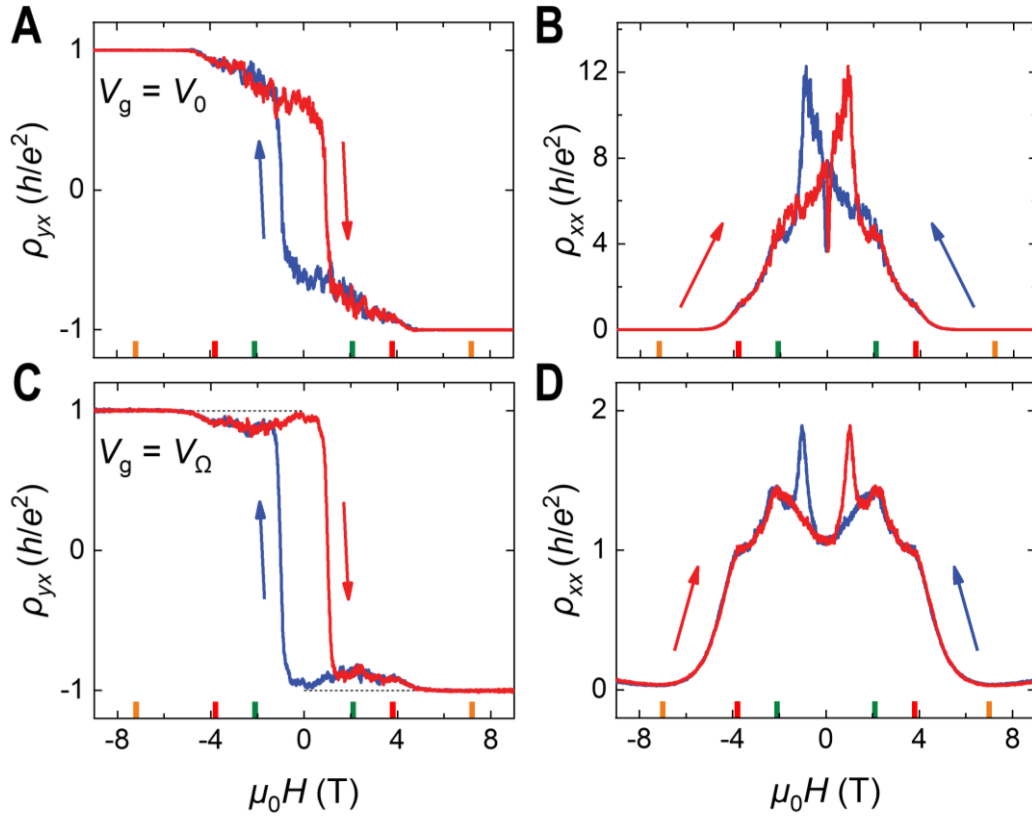


Fig. 2. QAH and r-QAH effect in a five-layer MnBi_2Te_4 thin film #1 at $T = 20$ mK. (A and B) Hysteretic ρ_{yx} and ρ_{xx} at V_0 as a function of $\mu_0 H$. The ZMF $|\rho_{yx}| \approx 0.6 h/e^2$ and $\rho_{xx} \approx 7.6 h/e^2$ are far from ZMF-QAH effect but common for few-layer MnBi_2Te_4 device. (C and D) Hysteretic ρ_{yx} and ρ_{xx} at V_Ω with respect to $\mu_0 H$. Orange, red, and green ticks dividing the curve into four stages, denote ± 7.2 T, ± 3.8 T, and ± 2.1 T, where $|\rho_{yx}| \approx 1.0, 0.9, 0.8 h/e^2$, and $\rho_{xx} \approx 0.04, 1.0, 1.3 h/e^2$, respectively. The ZMF $\rho_{yx} = 0.9736 h/e^2$ and $\rho_{xx} = 1.0756 h/e^2$ indicating a r-QAH effect. The data of ρ_{xx} and ρ_{yx} are already symmetrized and antisymmetrized.

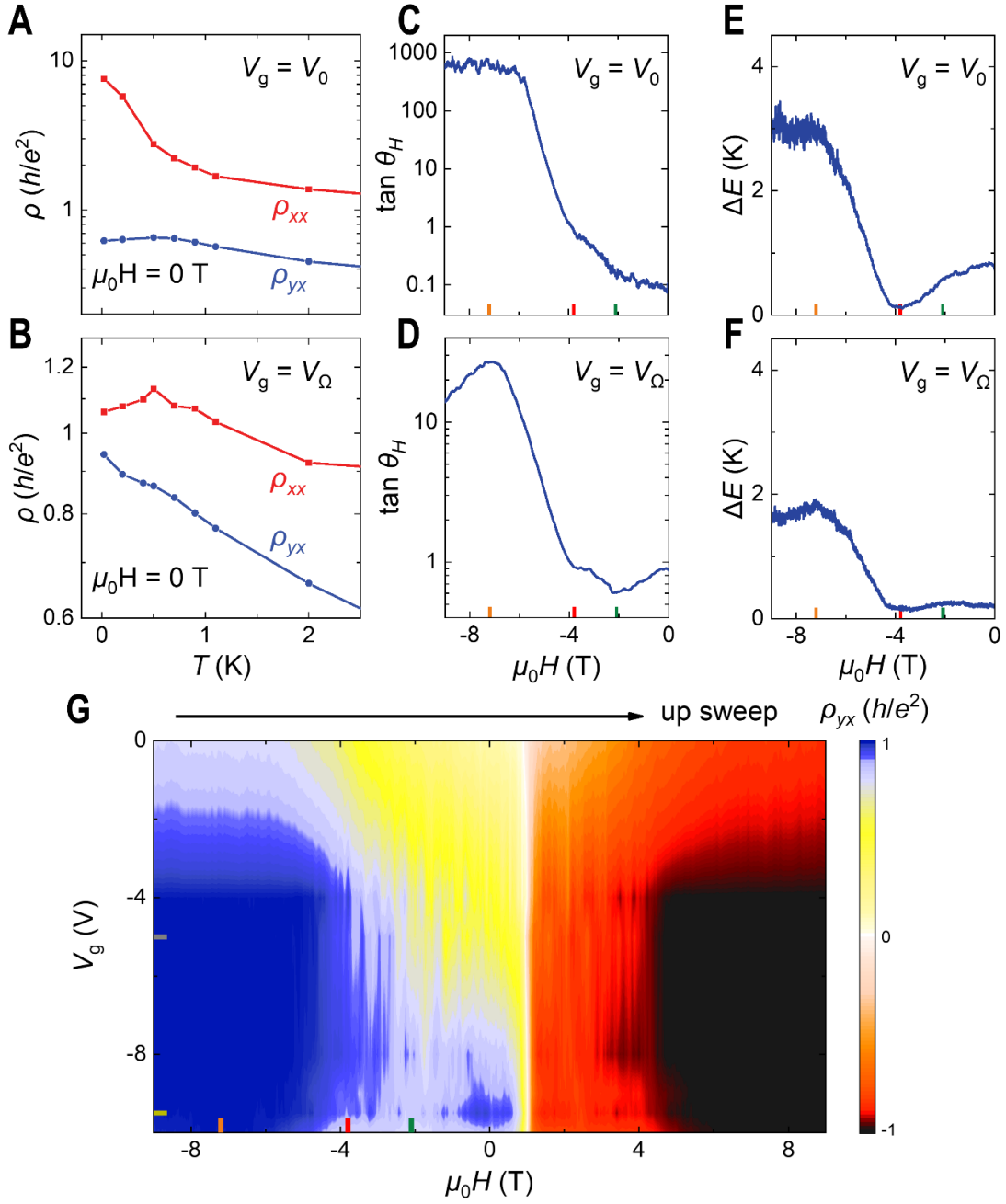


Fig. 3. Comparison of V_0 and V_Ω in the five-layer MnBi₂Te₄ thin film #1. (A and B) Temperature dependence of ρ_{xx} and ρ_{yx} for the ZMF-insulating state at V_0 and the CAI state at 0 T and V_Ω , respectively. (C and D) Tangent of Hall angle $\tan \theta_H = \sigma_{xy}/\sigma_{xx} = \rho_{yx}/\rho_{xx}$ as a function of $\mu_0 H$ for V_0 and V_Ω , respectively. Orange, red, and green ticks dividing the curve into four stages, denote -7.2 T, -3.8 T, and -2.1 T. (E and F) Effective energy gap ΔE as a function of $\mu_0 H$ for V_0 and V_Ω , respectively. ΔE is obtained from fitting the Arrhenius plots. (G) Intensity plot of ρ_{yx} with respect to $\mu_0 H$ and V_g which is collected during $\mu_0 H$ upsweep and subsequently antisymmetrized with downsweep data. Orange, red, and green tick denote -7.2 T, -3.8 T, and -2.1 T. Grey and gold tick denote V_0 and V_Ω , respectively. Three QAH regimes is observable: down-HMF-QAH regime ($\mu_0 H < -4$ T and $V_g < -2$ V), up-HMF-QAH regime ($\mu_0 H > +4$ T and $V_g < -2$ V), and r-QAH regime at 0 T and V_Ω in the bottom center.

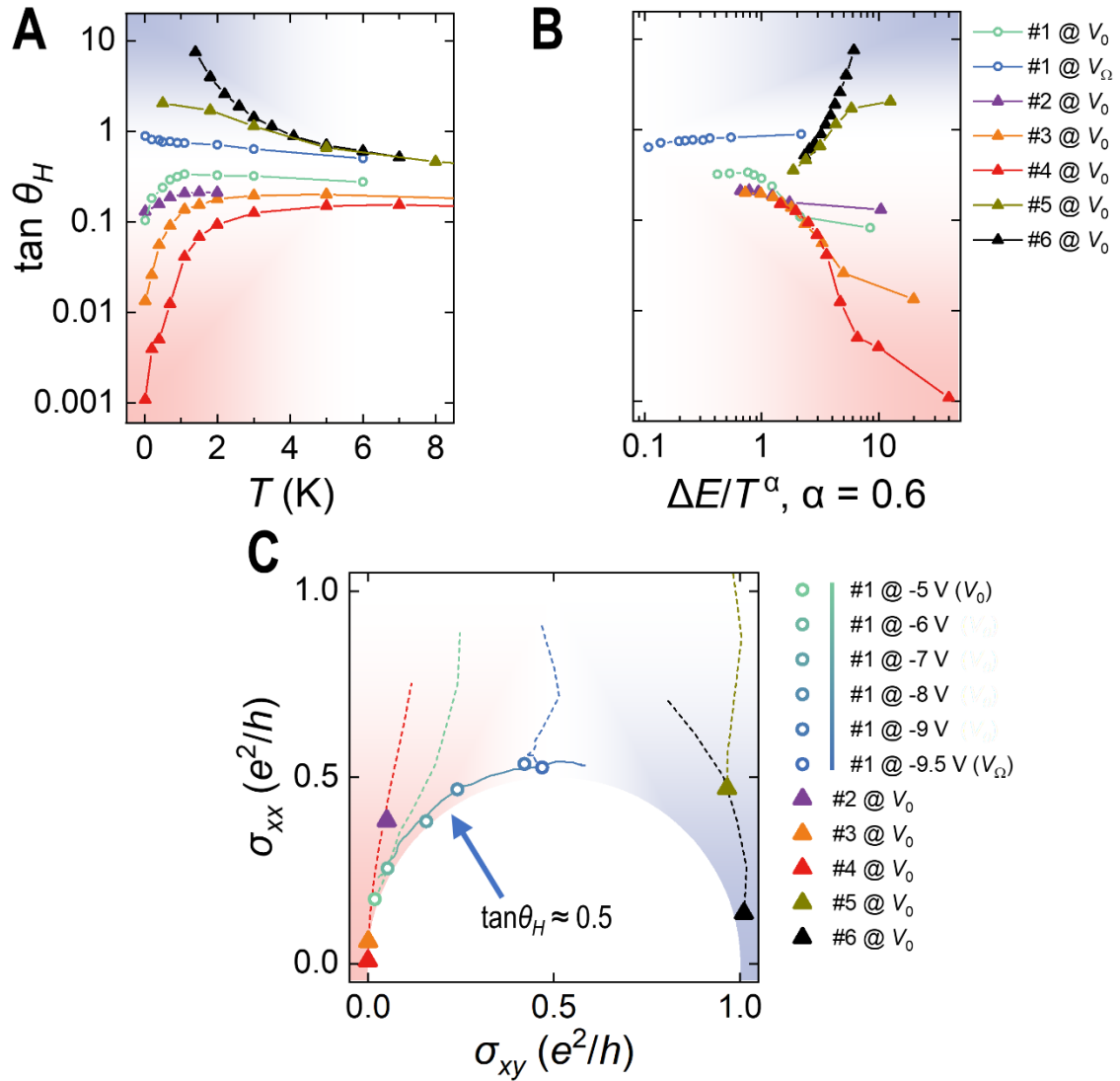


Fig. 4. Comparison of the five-layer MnBi₂Te₄ thin film #1 and other samples. (A) Temperature dependence of ZMF $\tan \theta_H$ for the thin film #1, additional thin films #2 #3 #4, and exfoliated flakes #5 #6. #5 is the seven-layer flake with ZMF-QAH effect under high pressure [52] and #6 is the five-layer flake with ZMF-QAH effect [6]. (B) Scaling analysis of $\tan \theta_H$ with respect to $T/\Delta E^\alpha$, where ΔE is at ZMF and $\alpha = 0.6 \pm 0.05$. At the transition point, the T -independent $\tan \theta_H \approx 0.5$, obtained from the well-collapsing curve of #2 to #6. (C) ZMF parametric plots of $(\sigma_{xy}(\beta), \sigma_{xx}(\beta))$ where β evolves T and V_g . Dashed lines denote the ZMF-RG flows in $(\sigma_{xy}(\beta), \sigma_{xx}(\beta))$ observed with changing T . Solid line denotes ZMF V_g sweep in #1 from V_0 to V_Ω . Open circles denote data extracted from $\mu_0 H$ sweep in thin film #1. Triangulars denote thin films #2, #3, #4, and thin flakes #5, #6. Blue arrow indicates the transition point obtained from T -independent $\tan \theta_H \approx 0.5$. The sky-blue and pink shaded area denote the QAH regime and ZMF-insulating regime, respectively.